Al-Doped Black Phosphorus p–n Homojunction Diode for High Performance Photovoltaic

*Yuanda Liu, Yongqing Cai, Gang Zhang, Yong-Wei Zhang, and Kah-Wee Ang**

2D layered materials based p–n junctions are fundamental building block for enabling new functional device applications with high efficiency. However, due to the lack of controllable doping technique, state-of-the-art 2D p–n junctions are predominantly made of van der Waals heterostructures or electrostatic gated junctions. Here, the authors report the demonstration of a spatially controlled aluminum doping technique that enables a p–n homojunction diode to be realized within a single 2D black phosphorus nanosheet for high performance photovoltaic application. The diode achieves a near-unity ideality factor of 1.001 along with an on/off ratio of ≈5.6×10^3 at a low bias of 2 V, allowing for low-power dynamic current rectification without signal decay or overshoot. When operated under a photovoltaic regime, the diode's dark current can be significantly suppressed. The presence of a built-in electric field additionally gives rise to temporal short-circuit current and open-circuit voltage under zero external bias, indicative of its enriched functionalities for self-powered photovoltaic and high signal-to-noise photodetection applications.

1. Introduction

Energy-band engineering in 2D layered materials is a key enabler for the realization of microelectronic devices including field-effect transistors[1–3] and p–n junctions.[4–7] The p–n junction diode presents the basic element of incumbent electronics and optoelectronics devices that can be employed for current rectification and energy harvesting. Recently, 2D layered materials based p–n junctions[5,8,9] have attracted tremendous attentions for the versatility in applications due to their promising mechanical, electrical, and optical properties. Spatially separated charge conversion was first formed in graphene by electrostatic doping, but it did not show diode-like functionalities due to Klein tunneling and its zero bandgap.[10] Although gate-modulated p–n homojunctions were later demonstrated in semiconducting transition-metal dichalcogenides (TMDCs)[4,5,7] and black phosphorus (BP)[11,12] sheets with tunable bandgaps, such diodes require complicated device structure and suffer from nonabrupt p–n interface due to the divergence of static electric field that prevents them for practical applications. In an alternative way, van der Waals heterojunctions constructed using TMDCs[6,13–16] and BP[17–19] have recently been developed by vertically staking the n- and p-nanoflakes. However, it is not always trivial to find materials with suitably aligned energy levels. In particular, contaminants and bubbles will be inevitably induced during the dry transfer process, resulting in defects that can act as carrier traps and recombination centers at the heterointerfaces. Another explored technique is the epitaxy of lateral heterojunctions composed of p- and n-type TMDCs semiconductors.[20–22] By alternating precursor vapors and adjusting the growth parameters, disparate materials can be nucleated and grown along the edges or on top of the as-grown crystals, resulting in heterojunctions. However, although the poor reproducibility and controllability of the growth process might be mitigated by upgrading the chemical vapor deposition system that relies on the optimized gas flow and temperature modulation, the challenges involve in the control of large-area uniform growth and the high yield of clean junction interface will unambiguously prohibit its practical use. Therefore, it would be highly desirable to form a homogenous p–n junction in a single 2D material that has both an abrupt junction interface and a high-quality single crystal carrier diffusion path, which will open up new realms of applications in nanoelectronic circuits, electroluminescence, and photovoltaics.

Comparing with semimetallic graphene, BP is a semiconductor with a tunable direct bandgap for all number of layers.[23,24] Its thickness-dependent bandgap is predicted from 2 eV for monolayer to 0.3 eV for bulk and can be further expanded to 0.15 eV by As doping, corresponding a broadband wavelength from 620 to 8265 nm.[25] BP has emerged as a promising material for optoelectronic devices given its ambipolar conduction, the anisotropic nature, the monoelemental composition, alongside with field-effect hole mobility of 300–1000 $cm^2\ V^{-1}\ s^{-1}$ that outperforms the TMDCs.[26–28] Furthermore, the conductivity type control in BP can be modified by forming covalent bonds with foreign dopants. Previous

Dr. Y. Liu, Prof. K.-W. Ang
Department of Electrical and Computer Engineering
National University of Singapore
4 Engineering Drive 3, 117583, Singapore
E-mail: eleakw@nus.edu.sg
Dr. Y. Liu
School of Electronic Science and Engineering
Nanjing University
Nanjing 210093, China
Dr. Y. Cai, Dr. G. Zhang, Prof. Y.-W. Zhang
Institute of Higher Performance Computing
1 Fusionopolis Way, 138632, Singapore

DOI: 10.1002/adfm.201604638

density functional theory (DFT) calculations predicted the formation of covalent bonds between the adsorbed nitric oxide and phosphorene,[29] suggesting that foreign atoms that have dangling bonds can be directly bond to BP. For instance, the phosphorene-carbon bonds[30] have been experimentally identified during the process of chemical passivation to black phosphorus. The strong bonds between phosphorus atoms and foreign dopants[31–34] offer comparative advantage over its main 2D competitor, graphene, which has robust and stable sp^2 carbon structure.[35] This allows flexibility in tuning the type and the concentration of dominant carriers in BP, thereby enabling devices that require both p- and n-type semiconductors such as p–n junction diodes to be realized. Moreover, comparing with the electrostatic modulation using the external electrical field, dopants doping provides a nonvolatile doping capability with the ease of device fabrication and stability of the device operation.

Here, we demonstrate a facile spatially controlled Al-doping technique that enables the realization of a near-ideal p–n homojunction diode within few-layer BP nanosheet. The electron mobility is found to be significantly increased up to ≈2.5 times, which leads to highly improved electron transport in n-type BP transistors. The diode achieves an ideality factor of 1.001, an on/off ratio higher than 10^3 together with a low reverse current in the order of nA, allowing low-power dynamic current rectification without signal decay or overshoot. The room-temperature photovoltaic response under near-infrared (NIR) 1550 nm wavelength excitation results in a maximum open-circuit responsivity of ≈15.7×10^3 V W^{-1} and short-circuit responsivity of ≈6.2 mA W^{-1}, which corresponds to an open-circuit voltage of ≈140 mV and short-circuit current of ≈6 mA cm^{-2}, respectively. The first demonstration of dynamic photovoltage and photocurrent generation in BP homojunction diode in the absence of external bias is envisioned to be important for self-powered photovoltaic and photodetection applications.

2. Results

2.1. Theoretical Band Structure of Al-Doped Phosphorene

We found that the Al atoms both at the surface adsorbed site and at the intercalated site would donate electrons to the host phosphorene, inducing n-type conductance in the Al-phosphorene system. These two cases are simulated using two models: monolayer phosphorene surface adsorbed by one Al atom and bilayer phosphorene intercalated by one Al atom. **Figure 1** shows the theoretical electronic structure of Al atom intercalated bilayer phosphorene performed by

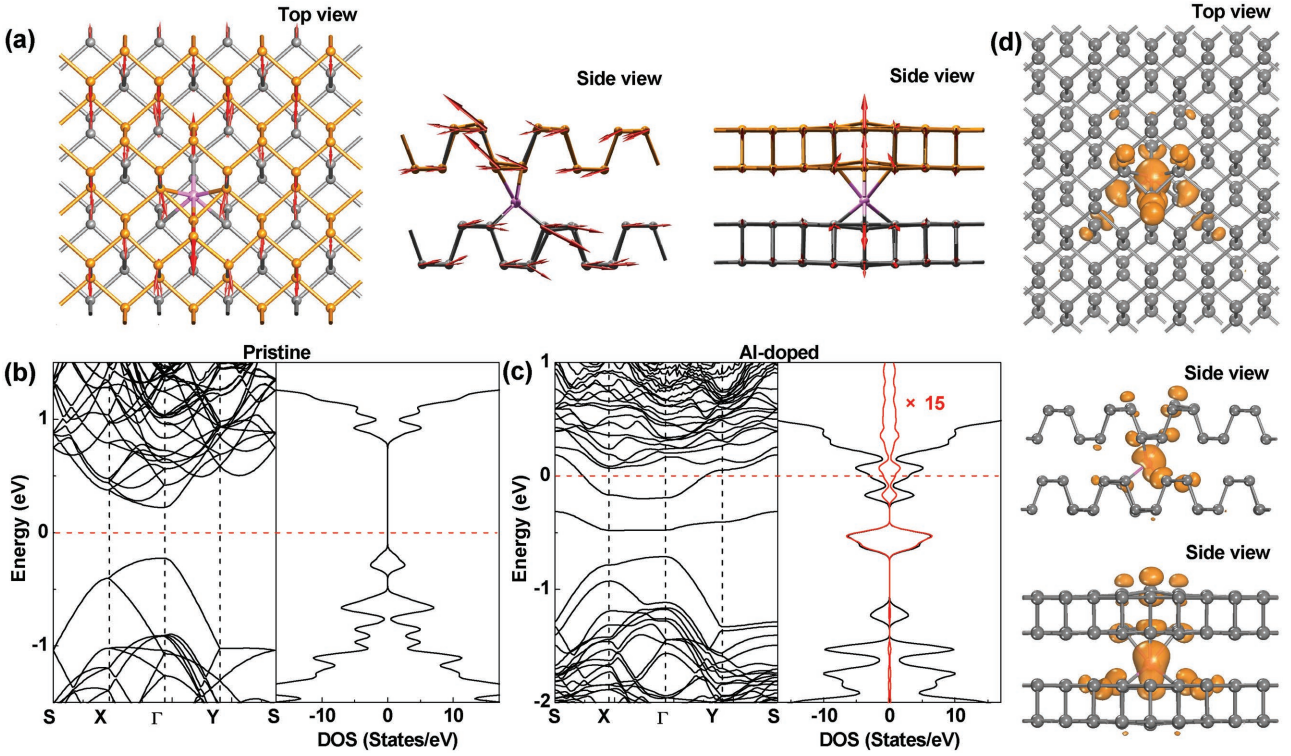

Figure 1. Theoretical electronic properties of Al-doping in bilayer phosphorene. a) Top and side views of Al atom (pink sphere) intercalated induced atomic displacements in bilayer phosphorene. The yellow (gray) spheres represent the phosphorus atoms in the top (bottom) layer. The red arrows indicate the displacement for each phosphorus atom. The size and length of the red arrows scale with the magnitude of the atomic displacement. b,c) First-principles electronic band structures (calculated with the GGA-PBE (generalized gradient approximation) method) and corresponding DOS (calculated with the HSE06 functional) for Al atom intercalated bilayer phosphorene, showing the donation of excess electrons due to Al doping which results in the upward shift of E_F (Fermi level) into the conduction band. The red dashed lines indicate the position of the E_F in phosphorene. The total DOS and local DOS of Al are represented by the black and red solid lines, respectively. d) Top and side views of the partial charge density of electrons distributed in the energy range $E_F - 0.6$ eV $< E < E_F$. Donation of electrons from the Al atom (pink sphere) and hybridization between orbitals of Al and phosphorus (gray sphere) are vividly depicted.

first-principles calculations (see Figure S1, Supporting Information, for monolayer phosphorene surface adsorbed by one Al atom). As shown in Figure 1a, the lowest-energy configuration of intercalated Al atom forms six covalent Al—P bonds with the neighboring phosphorus atoms with the bond lengths ranging from 2.39 to 2.61 Å. The binding energy (defined as $E_b = E_{Al+phosphorene} - E_{Al} - E_{phophorene}$) is calculated to be as strong as −2.21 eV. This relatively strong interaction is attributed to the hybridization of the Al atom with the lone electron pair in phosphorus atoms, allowing stable chemical doping in phosphorene and leading to large outward and in-plane atomic displacements of phosphorus atoms around the Al dopant (Figure 1a). The Al-doping results in a large broadening of the peaks of the P—P bond length distribution compared with pristine phosphorene (Figure S2b, Supporting Information). Figure 1b,c exhibits the electronic band structures as well as the corresponding density of states (DOS) of pristine and Al-doped bilayer phosphorene, respectively. Comparing with the E_F (Fermi level) of the pristine phosphorene that is in the middle of the bandgap, the E_F in Al-doped phosphorene shifts upwardly into the conduction band, or in other word, Al atom can act as an effective electron donor in the Al-phosphorene system. Bader charge analysis indicates that per Al atom donates around 1.7 electrons into the host lattice. The electronic coupling between the Al dopant and the host lattice is vividly reflected by the isosurface plot of the partial charge density integrated from E_F – 0.6 eV to E_F, as shown in Figure 1d.

2.2. Spatially Controlled Al-Doping for n-Type BP

Figure 2a illustrates the device structure of the n-type BP transistor. The few-layer BP flake was obtained by mechanical exfoliation and was used as the channel in a back-gate transistor. We n-dope the BP channel by Al atoms thermally diffusion (see the Experimental Section and the Supporting Information in detail). Al atoms diffuse into the BP, donating electrons to convert the BP segment from p- to n-type. Figure 2b presents a typical cross-sectional transmission electron microscope (TEM) image of the channel of the Al-doped BP transistor. Layered BP nanosheets with a clear interlayer separation of about 0.5 nm can be observed, indicating that the thin BP sheet with a thickness of about 2.5 nm can still preserve the high-crystalline characteristics after the device fabrication process. The presence of Al in BP lattice was confirmed by the energy-dispersive X-ray spectroscopy (EDX) spectrum (Figure 2c) taken along the red arrow shown in Figure 2b of the TEM image. Because Al atoms thermally diffuse into the host lattice, the concentration of Al

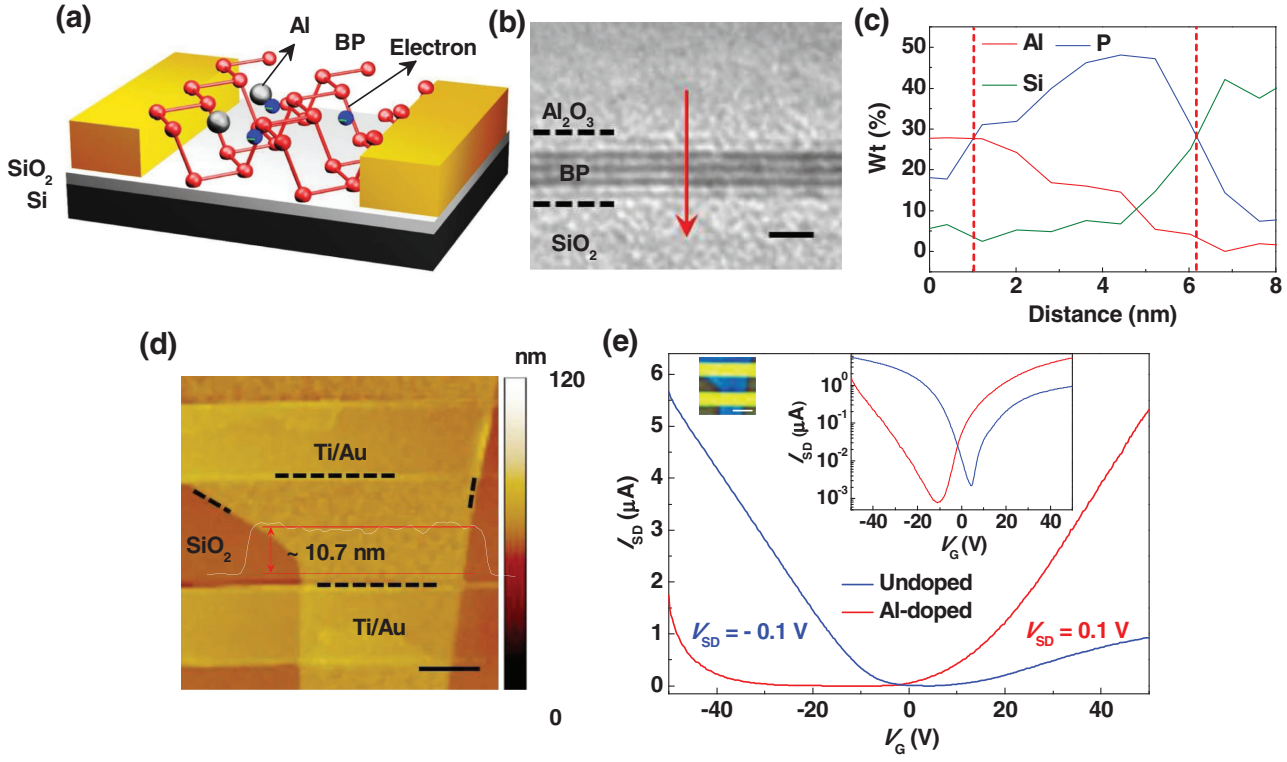

Figure 2. Characterization of Al-doped n-type few layer BP transistor. a) Schematic of the electron donation from Al atoms to the BP host lattice. The gray and the blue spheres represent the Al atoms and the electrons, respectively. b) High resolution cross-sectional TEM image of the Al-doped n-type BP channel. Scale bar, 2 nm. c) EDX elemental spectrum scanned along the red arrow shown in (b) of the TEM image, showing Al atoms diffusion into the BP channel. The area between the red dashes shows the elemental ratio in the BP sheet. d) AFM height image with a line scan profile of the Al-doped n-type FET (Scale bar, 1 μm). The black dashes show the edge of the BP channel. The thickness of the BP sheet is estimated to be about 10.7 nm. e) Transfer characteristics of the undoped p-type (V_{SD} = –0.1 V) and the Al-doped (V_{SD} = 0.1 V) n-type BP transistors. The inset depicts the same data on a logarithmic scale. The inset image is the optical image of the Al-doped BP FET (Scale bar, 2 μm). The gold areas indicate the metal electrodes. The blue areas and gray areas are BP sheet and SiO_2/Si substrate, respectively.

decreases with the thickness of the BP sheet, implying that the properties of the Al doped n-type transistor device can be optimized further. Figure 2e shows the transfer characteristics of another Al-doped two-terminal BP transistor device fabricated on the same substrate with the same process run. The thickness of the BP channel is estimated to be about 10.7 nm from the atomic force microscope (AFM) height image shown in Figure 2d. As can be seen from Figure 2e, comparing with the undoped BP transistor which exhibits p-type behavior with $I_{on}/I_{off} \approx 2.6 \times 10^3$, and V_{TH} (threshold voltage) of ≈4.5 V, the Al-doped BP transistor displays clearly n-type conductance with the $I_{on}/I_{off} \approx 6.6 \times 10^3$ and $V_{TH} \approx -10$ V, indicating that Al atoms doping is an effective approach to achieve n-type conductance in BP. The room-temperature electron mobility is estimated to be ≈105 $cm^2\ V^{-1}\ s^{-1}$, which is remarkably enhanced up to ≈2.5 times comparing with the counterpart of ≈41 $cm^2\ V^{-1}\ s^{-1}$ extracted from the undoped BP transistor (Figure S3, Supporting Information). Although the electron mobility from our two-probe device is an underestimate of the true mobility, it is still about five times higher than that employing Cs_2CO_3 (≈27 $cm^2\ V^{-1}\ s^{-1}$)[36] or Al contacts (≈24 $cm^2\ V^{-1}\ s^{-1}$ for two-probe device)[37] and is slightly higher than the results from the copper doped transistor (≈80 $cm^2\ V^{-1}\ s^{-1}$ at room temperature on SiO_2/Si substrate).[38]

2.3. BP p–n Homojunction Diode

The BP sheet employed for the p–n homojunction diode has a width of 5 μm and a length of 6 μm between the source and drain metal electrodes. To realize our p–n junction diode, half of the BP channel is defined by a second step EBL (E-Beam Lithography), followed by Al/Al_2O_3 deposition using Atomic Layer Deposition (ALD; see the Experimental Section) while leaving the other half unexposed. The thickness of the BP sheet is measured to be about 8.5 nm (Figure S4, Supporting Information). From the output plots shown in **Figure 3**a, it is observed that the device reveals typical rectifying behavior with gate tunability, indicating the operating mechanism of a p–n homojunction diode (Logarithmic scale of the same data is shown in Figure S5, Supporting Information). Note that the drain electrode in contact with n-type BP was grounded in all of the electrical measurements. Figure 3b depicts the gate-dependent rectification factor of the diode, which is defined as the ratio of the forward current I_F to the reverse current I_R at the same bias magnitude of 2 V. The rectification factor is about 5.6×10^3 at $V_G = -10$ V and increases as the back-gate voltage decreases. The reverse bias current is <1 nA up to $V_{SD} = -2$ V, representing promising characteristics for low-power electronics. As presented in the inset of Figure 3b, the ideality factor of the diode is extracted to be 1.001 at $V_G = -10$ V by fitting using the Shockley diode equation, showing a near-ideal p–n junction diode. Figure 3c,d presents the dynamic rectified V_{IN}–V_{OUT} curves of our diode at external resistance of 1 MΩ by applying the sinusoidal or square input voltage signal sweeps from −3 to 3 V at 10 Hz. We do not observe signal decay and overshoot, indicative of the steady rectification behavior. The transfer characteristics of the diode under forward bias of 0.3 V is shown in Figure 3e. A hump together with two valleys is notably present. The conductance for $V_G < -8.5$ V (regime I) decreases when the absolute value of gate voltage decreases. The conductance begins to increase until for $V_G = -4$ V (regime II) then becomes suppressed again for V_g between −4 and 1.5 V (regime III), after which the conductance increases monotonically with an increase in gate voltage (1.5 V < V_G < 50 V; regime IV). Comparing with the monotonic decrease or increase of the transfer curves for undoped and Al-doped BP transistor shown in Figure 2e, we can see that the hump structure is unique for the sample with p–n homojunction.

The BP nanosheet is doped into a p–n junction by Al atoms, and the gate voltage can further tune the doping concentrations of both semiconductors, thus allowing tunability in the potential barrier and the built-in electric field at the heterointerface. The current of the diode at negative gate voltage is higher than the counterpart at positive gate voltage, hence we can increase the forward current more effectively by applying a negative gate voltage. This implies that the hole concentration in p-type BP is higher than the electron concentration in n-type BP, as schematically depicted in the energy band diagram in the inset of Figure 3e. For regimes I, II, III, and IV in the I_{SD}–V_G plot, the diode works in the mode of p^+p^-, pn^-, p^-n, and nn^+, respectively (Figure 3f). In regime I, a high negative gate shifts the conduction band and valence band up relative to the Fermi level, causing degenerate hole doping in the p-type half BP channel and a small quantity of excess holes in the Al-doped half. In regime II, as the electrons in the Al-doped half is becoming the dominated carriers, the recombination between electrons and holes occurs at the depletion region near the homojunction, resulting in an increase of current. In regime III, as the holes concentration inside the p-half is being reduced due to an increase in gate voltage, the current began to decrease. When a high positive gate bias further enriches the electrons inside both semiconductors, the device then works in a nn^+ junction mode in regime IV, exhibits n-type semiconducting characteristics. As the p-half BP sheet is also envisioned to be doped as high as n-type by the gate (Figure S3, Supporting Information), it is expected to result in the lowest potential barrier offset among the four regimes, which may be the reason responsible for a high positive voltage but with a low $I_F/|I_R|$ ratio (as shown in Figure 3b).

2.4. Near-Infrared Photovoltaic Effect

Based on the understanding of the gate-tunable charge transport, we further explore the photoexcited carriers generation and separation characteristics at the p–n homojunction interface. A 1550 nm continuous laser diode was used as the light source. **Figure 4**a shows a schematic of the device structure. As presented in Figure 4b, we can see that under light illumination, I_{SD}–V_{SD} curves do not cross the zero current (voltage) point even when the applied voltage (current) is 0. The observed nonzero open-circuit voltage ($I_{SD} = 0$) and short-circuit current ($V_{SD} = 0$) phenomenon is the unique feature of the p–n homojunction as compared to photoconductive photodetector, suggesting that the homojunction diode is capable of photovoltaic energy conversion without any external power input and consumption. As shown in the inset of Figure 4b, we plot the

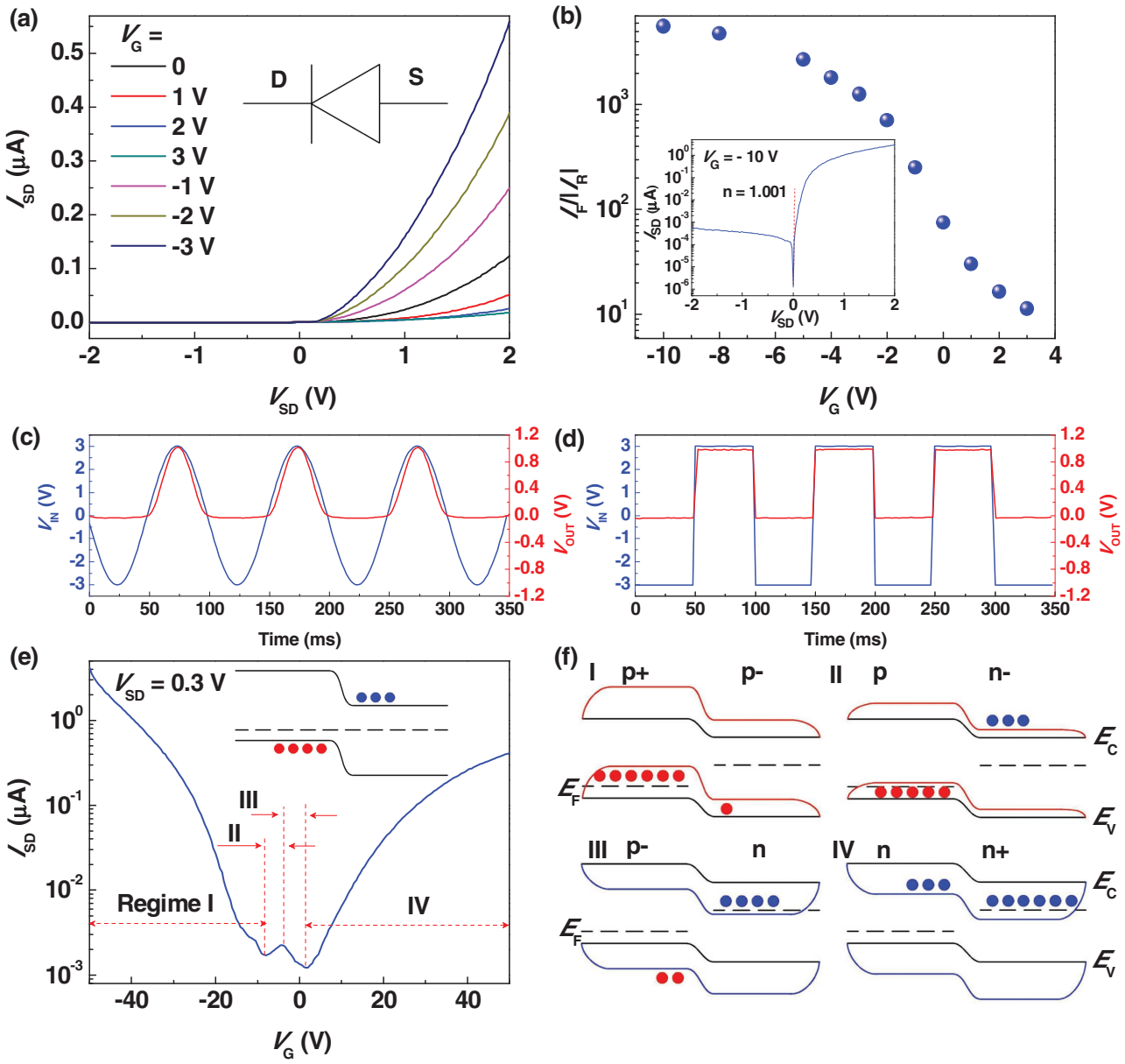

Figure 3. Gate controlled few-layer BP p–n homojunction diode and principle of operation. a) Gate-tunable rectifying output curves (I_{SD}–V_{SD}) of the device, showing unambiguously the presence of a p–n homojunction. b) Forward-to-reverse current ratio (at a homojunction bias magnitude of 2 V) as a function of gate voltage. The inset shows the logarithmic plot of the output characteristic under $V_G = -10$ V. The ideality was estimated to be 1.001 by fitting to Shockley diode equation, indicative of a near-ideal p–n junction diode. Shockley diode equation: $I_{SD} = I_0(\exp(V_{SD}/nV_T) - 1)$, where I_{SD} is the diode current; I_0 is diode reverse bias saturation current; V_{SD} is diode voltage; n is the diode ideality factor ($n = 1$ is ideal); and V_T is thermal voltage (≈25.85 mV at 300 K, calculated as $V_T = k_B T/q$, k_B is the Boltzmann constant, T is the temperature, and q is the electron charge). c,d) Demonstration of rectified dynamic output voltage using the few-layer BP homojunction diode by applying an AC sine wave and an AC square wave, respectively. The resistance of the series resistor is 1 MΩ. $V_{IN} = \pm 3$ V at 10 Hz. $V_G = -10$ V. e) Transfer curves (I_{SD}–V_G) of the p–n diode under forward bias of 0.3 V with back gate modulations, showing that the device is operating under holes dominated regime. The inset illustrates the bandgap diagram of the diode under zero bias and zero back-gate voltage. f) Schematic energy band diagrams of the diode under forward bias ($V_{SD} > 0$) for four doping configurations of the diode under back-gate modulation, which explains the gate voltage dependence of the potential barrier height and the built-in electric field. The black lines show the energy band under thermal equilibrium.

electrical power P_{el} as a function of the source–drain voltage under incident illumination of 451 nW. A maximum electrical output power of about 54.3 pW is obtained at $V_{max} = 0.08$ V. The corresponding current is $I_{max} = 67.9$ nA, and the dashed rectangle in Figure 4b shows the associated power area. The power conversion efficiency η_{PV} is estimated by $\eta_{PV} = P_{el,max}/P_{light}$, where P_{light} is the incident optical power. As the lateral junction does not cover all the area of the BP channel, we assume that the power conversion takes place in an intrinsic active area of 0.1 × 6 μm^2 near the junction interface and we can obtain

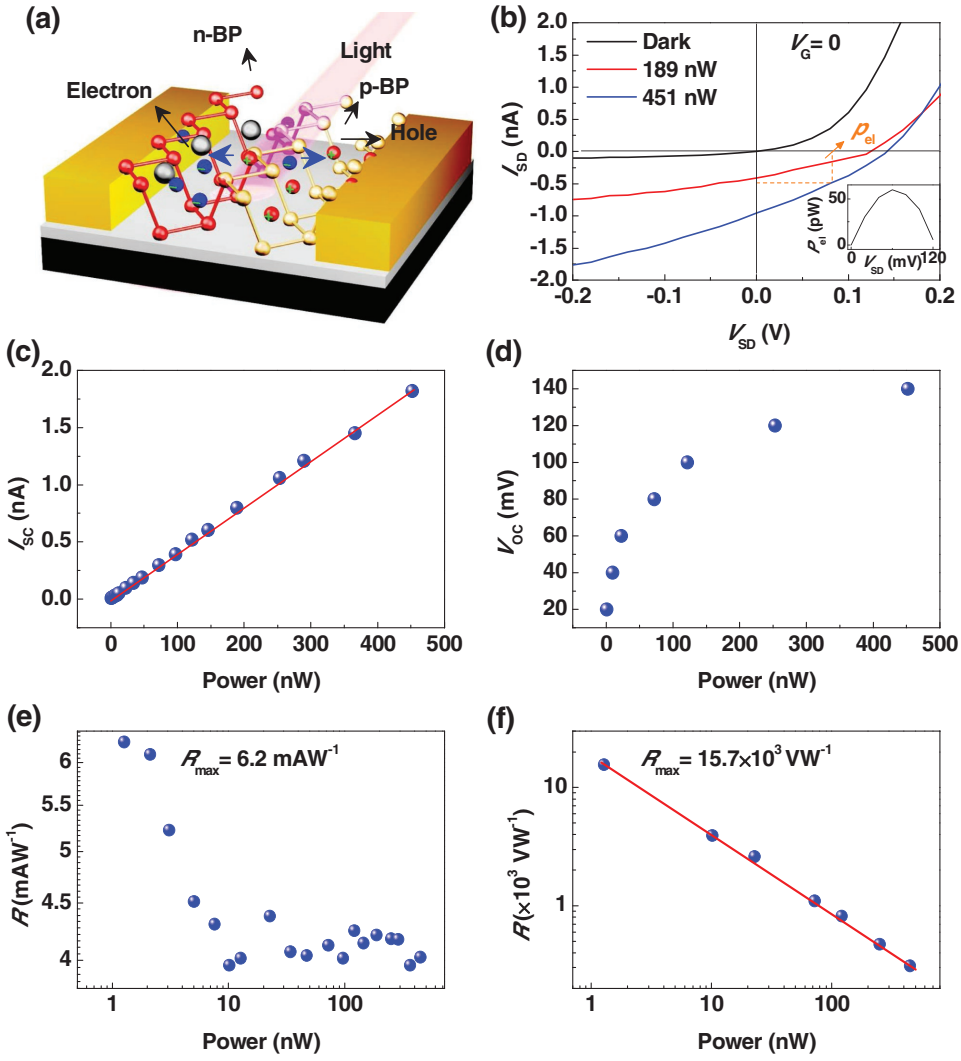

Figure 4. Device operation under photovoltaic effect. a) Schematic showing the separation of photogenerated electron–hole pairs due to the built-in electric field at the homojunction interface. The blue arrows show the electron and hole drift directions. The light source is a continuous laser diode operating at 1550 nm. b) I_{SD}–V_{SD} curves measured under dark and light illumination without gate modulation. The light source is a laser diode operating at 1550 nm. Short-circuit current and open-circuit voltage are produced under light illumination despite operating at $V_G = 0$ V. The inset shows the electrical power as a function of the source–drain voltage under the light illumination of 451 nW. Maximum conversion efficiency of ≈0.66% is obtained at $V_{SD} = 0.08$ V, $I_{SD} = 67.9$ nA. The yellow dashed line rectangle in the main panel shows the corresponding power area. c) Short-circuit current versus incident light power. The solid line is fitted to the experimental data. d) Open-circuit voltage versus incident light power. e,f) Photoresponsivity as a function of the incident light power. The maximum responsivity is extracted to be ≈6.2 mA W^{-1} and ≈15.7 × 10^3 V W^{-1}, respectively.

the power conversion efficiency of 0.66%. This value is slightly higher than that for WSe_2 p–n junction defined by the gate voltages ($\eta_{PV} = 0.5\%$).[5] The short circuit current increases linearly up to ≈6 mA cm^{-2} with the increase of the illumination power for $V_G = 0$ V, as shown in Figure 4c. The open-circuit voltage also increases sublinearly with the light intensity, and saturates when the value approaches ≈0.14 V, indicating that the potential barrier height is close to this value. As depicted in Figure 4e,f, we achieve a maximum photoresponsivity at low incident power, which is extracted to be ≈15.7 × 10^3 V W^{-1} and ≈6.2 mA W^{-1}, respectively. Despite the use of a thin BP thickness of about 8.5 nm in our device (Figure S4, Supporting Information), the photoresponsivity is enhanced up to about 20 times as compared to previous reported ≈0.3 mA W^{-1} from a gate-defined p–n junction formed within a 30 nm thick BP.[11] The photoresponsivity can be further improved for photodetecting applications. To this end, we can adopt the technologies that can expand the active light absorbing area or optimize the photocarrier collection efficiency, such as multiple interdigitated electrodes, a suitable reverse bias, or the construction of vertical p–n junction. Specific detectivity is another figure of merit for photodetectors, which is related to the sensitivity that a detector can distinguish from the background noise. The detectivity of our diode is calculated to be 1.04 × 10^{11} Jones at $V_{SD} = 5$ V, $V_G = -10$ V, and $P_{light} = 1.3$ nW (see the Supporting Information).

Due to the existence of the built-in electrical field at the junction interface, the photogenerated electron–hole pairs can be

effectively separated spatially. Electrons are driven to the p-type side while holes moved to the n-type side, thus generating a photovoltaic effect. The recombination probability for electrons and holes during the drift process to opposite electrodes would be greatly reduced, which is superior to photoconductive photodetector. Our diode can work with a zero dark current and a zero power consumption, which is an unique advantage of the p–n homojunction comparing with the diode formed by gate-tunable p–n junction,[11,12] thereby provides versatility in device fabrication, operation and better energy efficiency. In contrast to conventional phototransistor based on 2D materials,[39–43] the dark current is clearly suppressed which gives rise to improved signal/noise ratio and may find practical applications in low-noise spectroscopy, high resolution night version, and optical communications.

2.5. Dynamic Photovoltaic Response

The photovoltaic effects observed in the photoinduced *I*–*V* characteristics (Figure 4b) are directly applied to dynamic photovoltaic switching which enables us to dynamically harvest the light energy. The dynamic photovoltaic switching is used to measure values of short-circuit current and open-circuit voltage without an external power supply. **Figure 5**a,b shows the on/off short-circuit current and open-circuit voltage at an incident power of 860 nW (1550 nm; $V_G = 0$). After hundreds of on–off cycles, the signal is well retained, demonstrating good reliability and reversibility of our diodes. At the same experimental conditions, we did not observe any detectable I_{SC} and V_{OC} in a control device with a pristine BP channel. Figure 5c,d gives the high-resolution temporal response. The rise time and the fall time of V_{OC} at $V_G = 0$ are measured to be about 3 and 10 ms, respectively. The response time is comparable with the gate-defined BP p–n junction (rise time, 2 ms; fall time: 3 ms).[12] However, the channel of their device has to be tuned by two split gates, which is complicated for the device operation. The dynamic photovoltaic switching without any electrical power consumption enables us to harvest light energy at a more efficient and facile manner, which is not possible for the gate-defined structures. The response speed can be further improved by applying a reverse source–drain voltage to the diode, allowing the application of high-speed photodetecting. The unique features of our diodes are the sensitivity to external electrostatic in BP conductivity, the efficient separation of the NIR photoexcited electron–hole pairs, the record high electron mobility inside the Al-doped segment, the broadband and linear-dichroism photon absorption.

3. Conclusion

In summary, we have demonstrated a p–n homojunction diode in few-layer black phosphorus that exhibits efficient photovoltaic behavior. We showed theoretically and experimentally the effectiveness of Al atoms as electron donors to transform

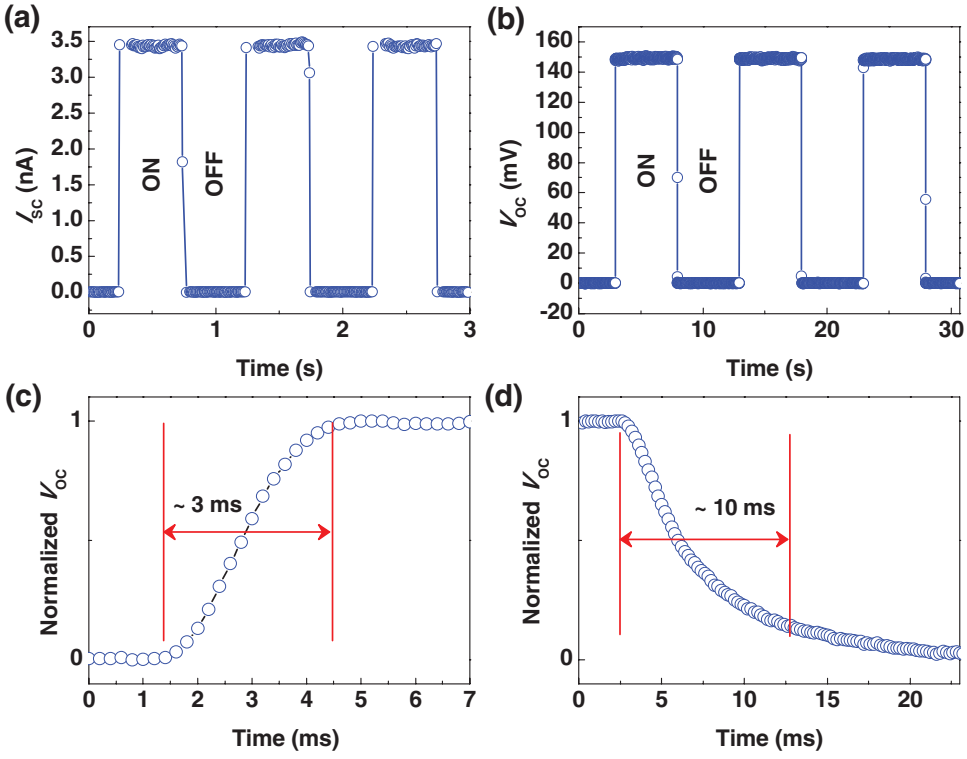

Figure 5. Temporal photovoltaic characteristics. a,b) Temporal nonzero short-circuit current I_{SC} and open-circuit voltage V_{OC} measured at a $V_G = 0$ V. The laser illumination power is ≈860 nW. Our diode is capable of harvesting NIR light energy dynamically. c,d) The rise time and fall time of the open-circuit voltage V_{OC} are estimated to be 3 and 12 ms, respectively.

the undoped p-type BP into n-type conductance. The electron mobility is significantly increased up to ≈2.5 times, leading to improved electron transport in n-type BP transistor. The existence of a built-in electric field efficiently separates the photoexcited electron–hole pairs without any external bias, leading to high performance near-infrared photovoltaic with an open-circuit voltage responsivity of $\approx 15.7 \times 10^3$ V W^{-1} and a short-circuit current responsivity of ≈6.2 mA W^{-1} at room temperature. This results in the first-of-its-kind self-powered dynamic photovoltage and photocurrent generation. Our first demonstration of BP p–n homojunction diode using a practical, facile, and controllable doping technique may pave the way for high performance photovoltaic and near-infrared photodetection applications.

4. Experimental Section

Device Fabrication: Few-layer black phosphorus were mechanically exfoliated from bulk single-crystal BP (purity 99.998%, HQ graphene) onto 300 nm thermal oxide on a degenerately p-type doped Si substrate. Exfoliation and subsequent fabrication procedures where BP was unprotected (for example, uncovered with Polymethyl-methacrylate (PMMA) or Al_2O_3) were performed in an argon-filled glove box with an O_2 and H_2O concentration less than 1 p.p.m. (parts per million). The few-layer BP sheets having micrometer footprint were contacted with thermally evaporated Ti/Au (60 nm/20 nm) that was patterned by standard electron-beam lithography. A second step of electron-beam lithography defined a local area covering the BP region to be exposed for Al-doping. Next, a 1 nm Al layer and 10 nm Al_2O_3 layer were deposited at 120 °C using both trimethylaluminum and water precursors in an atomic layer deposition system with vacuum chamber attached to an argon-filled glove box.

Electrical and Photoresponse Measurements: The electrical measurements were carried out in a closed cycle cryogenic vacuum probe station (≈10^{-6} mbar) and the data were collected by an Agilent B1500A semiconductor parameter analyzer. All measurements were performed at room temperature. For photoresponse characterization, the light excitation of 1550 nm was provided by laser diodes operated in continuous wave mode. The beam was guided through an optical fiber with a FC/PC ferrule and was subsequently incident onto the channel of the devices without focusing. The beam at the device was measured to be Gaussian shaped with a diameter of about 300 µm at 660 nm illumination. The area of the channel was <10 µm × 10 µm. Therefore, the photoresponsivity was calculated by normalizing with the incident light intensity that overlaps with the channel area.

AFM: AFM scans were acquired using a Bruker Dimension FastScan microscope operated in the tapping mode. Between the scans the BP samples were kept under atmosphere in a class 1000 clean room with controlled 50% relative humidity.

TEM and EDX: TEM images and EDX spectrum were taken with a JEOL-2010 transmission electron microscopy with an acceleration voltage of 200 kV.

Computational Details: First-principles calculations within the framework of DFT were performed by using Vienna ab initio simulation package.[44] Spin-polarized calculations using the projector augmented wave method with both the Perdew–Burke–Ernzerhof (PBE) functional and hybrid functionals (HSE06) were performed with a cutoff energy of 350 eV. van der Waals interactions were considered by using DFT-D2 method. The relaxed lattice constants of the bilayer phosphorene was a = 3.338 Å and b = 4.514 Å. The authors simulated the effect of Al dopant by introducing an Al atom into the van der Waals gap of bilayer phosphorene with a 4 × 3 supercell. A vacuum layer of 15 Å normal to the surface and a 3 × 3 × 1 Monkhorst–Pack grid for k-point sampling were adopted. All the structures were fully relaxed until the force exerted on the atoms were less than 0.01 eV Å^{-1}.

Supporting Information

Supporting Information is available from the Wiley Online Library or from the author.

Acknowledgements

This research was supported by the National University of Singapore Faculty Research Committee Grants (R-263-000-B21-133 and R-263-000-B21-731), A*STAR Science and Engineering Research Council Grant (Nos. 152-70-00013 and 152-70-00017), National Research Foundation Competitive Research Program (NRF-CRP15-2015-01), and by the National Research Foundation, Prime Minister's Office, Singapore under its medium sized center program. Y.L. acknowledges funding of the International Postdoctoral Exchange Fellowship Program (20150023), the National Natural Science Foundation of China (61504056), the China Postdoctoral Science Foundation (2014M551558), and Jiangsu Planned Projects for Postdoctoral Research Funds (1402028B).

Received: September 7, 2016
Revised: November 18, 2016
Published online: January 3, 2017

[1] K. S. Novoselov, A. K. Geim, S. V. Morozov, D. Jiang, Y. Zhang, S. V. Dubonos, I. V. Grigorieva, A. A. Firsov, *Science* **2004**, *306*, 666.
[2] B. Radisavljevic, A. Radenovic, J. Brivio, V. Giacometti, A. Kis, *Nat. Nanotechnol.* **2011**, *6*, 147.
[3] L. Li, Y. Yu, G. J. Ye, Q. Ge, X. Ou, H. Wu, D. Feng, X. H. Chen, Y. Zhang, *Nat. Nanotechnol.* **2014**, *9*, 372.
[4] J. S. Ross, P. Klement, A. M. Jones, N. J. Ghimire, J. Yan, D. Mandrus, T. Taniguchi, K. Watanabe, K. Kitamura, W. Yao, *Nat. Nanotechnol.* **2014**, *9*, 268.
[5] A. Pospischil, M. M. Furchi, T. Mueller, *Nat. Nanotechnol.* **2014**, *9*, 257.
[6] C. H. Lee, G. H. Lee, A. M. van der Zande, W. Chen, Y. Li, M. Han, X. Cui, G. Arefe, C. Nuckolls, T. F. Heinz, *Nat. Nanotechnol.* **2014**, *9*, 676.
[7] B. W. H. Baugher, H. O. H. Churchill, Y. Yang, P. Jarillo Herrero, *Nat. Nanotechnol.* **2014**, *9*, 262.
[8] H. Li, D. Lee, D. Qu, X. Liu, J. Ryu, A. Seabaugh, W. J. Yoo, *Nat. Commun.* **2015**, *6*, 6564.
[9] Y. Zhang, T. Oka, R. Suzuki, J. Ye, Y. Iwasa, *Science* **2014**, *344*, 725.
[10] N. Stander, B. Huard, D. Goldhaber-Gordon, *Phys. Rev. Lett.* **2009**, *102*, 026807.
[11] H. Yuan, X. Liu, F. Afshinmanesh, W. Li, G. Xu, J. Sun, B. Lian, A. G. Curto, G. Ye, Y. Hikita, *Nat. Nanotechnol.* **2015**, *10*, 707.
[12] M. Buscema, D. J. Groenendijk, G. A. Steele, H. S. van der Zant, A. Castellanos-Gomez, *Nat. Commun.* **2014**, *5*, 4651.
[13] A. Nourbakhsh, A. Zubair, M. S. Dresselhaus, T. Palacios, *Nano Lett.* **2016**, *16*, 1359.
[14] T. Roy, M. Tosun, X. Cao, H. Fang, D.-H. Lien, P. Zhao, Y.-Z. Chen, Y.-L. Chueh, J. Guo, A. Javey, *ACS Nano* **2015**, *9*, 2071.
[15] Y. Gong, S. Lei, G. Ye, B. Li, Y. He, K. Keyshar, X. Zhang, Q. Wang, J. Lou, Z. Liu, R. Vajtai, W. Zhou, P. M. Ajayan, *Nano Lett.* **2015**, *15*, 6135.
[16] M. M. Furchi, A. Pospischil, F. Libisch, J. Burgdörfer, T. Mueller, *Nano Lett.* **2014**, *14*, 4785.
[17] L. Ye, H. Li, Z. Chen, J. Xu, *ACS Photonics* **2016**, *3*, 692.
[18] P. J. Jeon, Y. T. Lee, J. Y. Lim, J. S. Kim, D. K. Hwang, S. Im, *Nano Lett.* **2016**, *16*, 1293.
[19] T. Hong, B. Chamlagain, T. Wang, H.-J. Chuang, Z. Zhou, Y.-Q. Xu, *Nanoscale* **2015**, *7*, 18537.

[20] X.-Q. Zhang, C.-H. Lin, Y.-W. Tseng, K.-H. Huang, Y.-H. Lee, *Nano Lett.* **2014**, *15*, 410.
[21] C. Huang, S. Wu, A. M. Sanchez, J. J. Peters, R. Beanland, J. S. Ross, P. Rivera, W. Yao, D. H. Cobden, X. Xu, *Nat. Mater.* **2014**, *13*, 1096.
[22] X. Duan, C. Wang, J. C. Shaw, R. Cheng, Y. Chen, H. Li, X. Wu, Y. Tang, Q. Zhang, A. Pan, *Nat. Nanotechnol.* **2014**, *9*, 1024.
[23] V. Tran, R. Soklaski, Y. Liang, L. Yang, *Phys. Rev. B* **2014**, *89*, 235319.
[24] J. Qiao, X. Kong, Z.-X. Hu, F. Yang, W. Ji, *Nat. Commun.* **2014**, *5*, 4475.
[25] B. Liu, M. Köpf, A. N. Abbas, X. Wang, Q. Guo, Y. Jia, F. Xia, R. Weihrich, F. Bachhuber, F. Pielnhofer, *Adv. Mater.* **2015**, *27*, 4423.
[26] X. Ling, H. Wang, S. Huang, F. Xia, M. S. Dresselhaus, *Proc. Natl. Acad. Sci. USA* **2015**, *112*, 4523.
[27] A. Castellanos-Gomez, *J. Phys. Chem. Lett.* **2015**, *6*, 4280.
[28] F. Xia, H. Wang, Y. Jia, *Nat. Commun.* **2014**, *5*, 4458.
[29] L. Kou, T. Frauenheim, C. Chen, *J. Phys. Chem. Lett.* **2014**, *5*, 2675.
[30] C. R. Ryder, J. D. Wood, S. A. Wells, Y. Yang, D. Jariwala, T. J. Marks, G. C. Schatz, M. C. Hersam, *Nat. Chem.* **2016**, *8*, 597.
[31] Y. Pan, Y. Wang, M. Ye, R. Quhe, H. Zhong, Z. Song, X. Peng, D. Yu, J. Yang, J. Shi, J. Lu, *Chem. Mater.* **2016**, *28*, 2100.
[32] I. Khan, J. Hong, *New J. Phys.* **2015**, *17*, 023056.
[33] T. Hu, J. Hong, *J. Phys. Chem. C* **2015**, *119*, 8199.
[34] Y. Ding, Y. Wang, *J. Phys. Chem. C* **2015**, *119*, 10610.
[35] A. K. Geim, K. S. Novoselov, *Nat. Mater.* **2007**, *6*, 183.
[36] D. Xiang, C. Han, J. Wu, S. Zhong, Y. Liu, J. Lin, X.-A. Zhang, W. Ping Hu, B. Özyilmaz, A. H. C. Neto, A. T. S. Wee, W. Chen, *Nat. Commun.* **2015**, *6*, 6485.
[37] D. J. Perello, S. H. Chae, S. Song, Y. H. Lee, *Nat. Commun.* **2015**, *6*, 7809.
[38] S. P. Koenig, R. A. Doganov, L. Seixas, A. Carvalho, J. Y. Tan, K. Watanabe, T. Taniguchi, N. Yakovlev, A. Castro Neto, O. Barbaros, *Nano Lett.* **2016**, *16*, 2145.
[39] Q. Guo, A. Pospischil, M. Bhuiyan, H. Jiang, H. Tian, D. Farmer, B. Deng, C. Li, S.-J. Han, H. Wang, Q. Xia, T.-P. Ma, T. Mueller, F. Xia, *Nano Lett.* **2016**, *16*, 4648.
[40] M. Buscema, D. J. Groenendijk, S. I. Blanter, G. A. Steele, H. S. van der Zant, A. Castellanos-Gomez, *Nano Lett.* **2014**, *14*, 3347.
[41] G. Konstantatos, M. Badioli, L. Gaudreau, J. Osmond, M. Bernechea, F. P. G. de Arquer, F. Gatti, F. H. L. Koppens, *Nat. Nanotechnol.* **2012**, *7*, 363.
[42] F. Xia, T. Mueller, Y. Lin, A. Valdes Garcia, P. Avouris, *Nat. Nanotechnol.* **2009**, *4*, 839.
[43] O. L. Sanchez, D. Lembke, M. Kayci, A. Radenovic, A. Kis, *Nat. Nanotechnol.* **2013**, *8*, 497.
[44] G. Kresse, J. Furthmüller, *Phys. Rev. B* **1996**, *54*, 11169.